Clim Dyn (2012) 38:2191–2207
DOI 10.1007/s00382-011-1087-0

Tropical intraseasonal rainfall variability in the CFSR

Jiande Wang · Wanqiu Wang · Xiouhua Fu · Kyong-Hwan Seo

Received: 15 January 2011 / Accepted: 23 April 2011 / Published online: 11 May 2011

Abstract While large-scale circulation fields from atmospheric reanalyses have been widely used to study the tropical intraseasonal variability, rainfall variations from the reanalyses are less focused. Because of the sparseness of in situ observations available in the tropics and strong coupling between convection and large-scale circulation, the accuracy of tropical rainfall from the reanalyses not only measures the quality of reanalysis rainfall but is also to some extent indicative of the accuracy of the circulations fields. This study analyzes tropical intraseasonal rainfall variability in the recently completed NCEP Climate Forecast System Reanalysis (CFSR) and its comparison with the widely used NCEP/NCAR reanalysis (R1) and NCEP/DOE reanalysis (R2). The R1 produces too weak rainfall variability while the R2 generates too strong westward propagation. Compared with the R1 and R2, the CFSR produces greatly improved tropical intraseasonal rainfall variability with the dominance of eastward propagation and more realistic amplitude. An analysis of the relationship between rainfall and large-scale fields using composites based on Madden-Julian Oscillation (MJO) events shows that, in all three NCEP reanalyses, the moisture convergence leading the rainfall maximum is near the surface in the western Pacific but is above 925 hPa in the eastern Indian Ocean. However, the CFSR produces the strongest large-scale convergence and the rainfall from CFSR lags the column integrated precipitable water by 1 or 2 days while R1 and R2 rainfall tends to lead the respective precipitable water. Diabatic heating related to the MJO variability in the CFSR is analyzed and compared with that derived from large-scale fields. It is found that the amplitude of CFSR-produced total heating anomalies is smaller than that of the derived. Rainfall variability from the other two recently produced reanalyses, the ECMWF Re-Analysis Interim (ERAI), and the Modern Era Retrospective-analysis for Research and Applications (MERRA), is also analyzed. It is shown that both the ERAI and MERRA generate stronger rainfall spectra than the R1 and more realistic dominance of eastward propagating variance than R2. The intraseasonal variability in the MERRA is stronger than that in the ERAI but weaker than that in the CFSR and CMORPH.

J. Wang (✉)
I.M. System Group Inc. at NOAA/NCEP/EMC, Camp Springs, MD, USA
e-mail: jiande.wang@noaa.gov

W. Wang
NOAA/NCEP/CPC, Camp Springs, MD, USA

X. Fu
IPRC, SOEST, University of Hawaii at Manoa, Honolulu, HI, USA

K.-H. Seo
Department of Atmospheric Sciences, Pusan National University, Busan, Korea

1 Introduction

Atmospheric reanalyses have been used to document the characteristics of the tropical intraseasonal variability that is dominated by the Madden-Julian Oscillation (MJO) (CLIVAR Madden–Julian Oscillation Working Group 2009), to diagnose the related physical processes (Shinoda et al. 1999; Kemball-Cook and Weare 2001), to initialize dynamical MJO prediction (Hendon et al. 2000; Saha et al. 2006; Fu et al. 2009; Kang and Kim 2010), to develop statistical forecast models (Jones et al. 2004; Seo et al. 2009), and to validate simulations and predictions by

numerical models (Seo et al. 2009; Kim et al. 2009). While the MJO involves large-scale dynamical processes and convective activities, condensational heating and the resulting rainfall from the reanalyses are generally considered less reliable than large-scale fields and are not used for diagnostic analyses and for validations of model simulations and predictions (Waliser et al. 2003; Lin et al. 2004; Wu et al. 2008). Because of the mutual interactions between large-scale circulations and convections, however, the incorrect rainfall in the reanalysis also implies the inaccuracy of the dynamical fields and their use for the MJO diagnostics may have consequently hindered our understanding of the MJO dynamics. Further, the initialization from inaccurate reanalyses may result in inferior MJO forecasting skill.

Shinoda et al. (1999) compared variability in observed outgoing longwave radiation (OLR) from satellite retrievals with that from the NCEP/NCAR reanalysis (R1, Kalnay et al. 1996) and showed that the amplitude of observed tropical intraseasonal convective variance in terms of OLR can be six times as large as that in the R1. The weak amplitude of convective activities in the R1 suggests that its intraseasonal components of dynamical large-scale prognostic variables may be also too weak and their enhancement may improve intraseasonal prediction initialized from the R1. This was confirmed by Fu et al. (2009) and Fu et al. (2010) who showed that the prediction skill of tropical intraseasonal variability strongly depends on initial conditions and amplifications of initial intraseasonal components in the R1 and the NCEP/DOE reanalysis (R2, Kanamitsu et al. 2002) resulted in an improved prediction skill. Likewise, the study of Janowiak et al. (2010) suggested strong dependence of the MJO prediction on initial conditions. These results indicate that improvements in the tropical large-scale circulation fields in the reanalyses are highly desirable for reliable diagnoses and predictions of the intraseasonal variability. Given the strong coupling between the convection and large-scale environment in the tropics, a reanalysis of better rainfall representation without explicitly assimilating observed precipitation is expected to have more accurate large-scale circulation fields.

Realistic simulations of the MJO remain a serious challenge for contemporary global climate models. Most of the models simulate too strong local persistence of equatorial rainfall and too weak eastward-propagating MJO rainfall signal (Lin et al. 2006; Zhang et al. 2006). Simulations of the MJO by general circulation models (GCMs) depend on various model physics (Zhang 2005). In particular, use of more restrictive criteria for the onset of convection results in stronger amplitude of the simulated MJO (Tokioka et al. 1986; Wang and Schlesinger 1999; Lin et al. 2008; Seo and Wang 2010). The need of a convection criterion in cumulus parameterizations to allow an accumulation of moist static energy before the start of the convection and is consistent with the observational evidence that a moisture buildup leads the onset of deep cumulus convection related to the MJO (Kemball-Cook and Weare 2001; Agudelo et al. 2006; Benedict and Randall 2007). Vertical heating profile was also found to be critical for the evolution of the MJO with maximum heating at higher levels corresponding to faster speed of eastward propagation of the MJO (Lau and Peng 1987; Chang and Lim 1988; Li et al. 2009). Lin et al. (2004) found that the vertical heating profile related to the MJO in the observational estimate is very top heavy with a westward tilt due to stratiform heating in the upper troposphere warming and possible shallow convective heating to the east of the deep convection. The importance of stratiform heating in the MJO evolution is further confirmed in modeling studies by Fu and Wang (2009) and Seo and Wang (2010). Lin et al. (2004) compared vertical heating profiles between GCM simulations and observational estimates and found that GCMs generally simulated a middle-heavy heating profile with insufficient heating in the upper troposphere and excessive heating in the lower troposphere. Jiang et al. (2009) showed that the diabatic heating in the European Centre for Medium-Range Weather Forecasts (ECMWF) reanalyses and forecasts is too strong and too deep compared to observational estimates based on the Tropical Rainfall Measuring Mission (TRMM). The recent study of Ling and Zhang (2011) revealed that there exist large discrepancies in diabatic heating among TRMM retrievals and global reanalyses. These results indicate that while a reasonable representation of the heating profile is of critical importance for a realistic MJO simulation, its representation in the reanalyses and numerical simulations/forecasts remain quite uncertain.

In this study we analyze intraseasonal rainfall variability in the recently developed NCEP Climate Forecast System Reanalysis (CFSR) and its comparison with the two previous NCEP reanalyses R1 and R2. The variability of rainfall, precipitable water (PWAT) and moisture convergence related to the MJO is analyzed to compare the relationship between rainfall and large-scale fields among the three NCEP reanalyses. Diabatic heating profiles from CFSR is examined to assess its representation of the physical processes related to the intraseasonal variability and possible implications of the model physics. In addition, rainfall variability from two other new reanalyses, the ECMWF Re-Analysis Interim (ERAI), and the Modern Era Retrospective-analysis for Research and Applications (MERRA), is also assessed. We aim to address the following questions: (1) how does the intraseasonal rainfall variability in the new generation of the reanalyses compare with the previous versions; (2) to what extent does the relationship between large-scale fields and rainfall differ

among the reanalyses, and what is the relevance of the difference to the dynamics of the MJO; and (3) how different is the heating directly generated in the reanalysis from that implied by the changes in large scale circulation and what are the implications to the model physics?

The reanalyses and observational validation data are described in Sect. 2. Results of the comparisons among the reanalyses and observations, MJO-related variability in NCEP reanalyses, and diabatic heating profiles from the CFSR are presented in Sect. 3 and are discussed in Sect. 4. A summary is provided in Sect. 5.

2 Data and methodology

Observations used in this study include the rainfall estimate for 2000–2009 from the satellite-based CPC MORPHing technique (CMORPH, Joyce et al. 2004) and outgoing longwave radiation (OLR) for 1979–2009 from the NOAA AVHRR (Liebmann and Smith 1996). Rainfall data for 2000–2009 from the reanalyses will be compared with CMORPH observation to assess the realism of intraseasonal variability in these reanalyses. While a full analysis of the related dynamical fields for all reanalyses is beyond the scope of this study, rainfall and circulation fields including horizontal winds, specific humidity, and PWAT from R1, R2, and CFSR will be used to analyze MJO-related variability. The analysis of these fields will be based on the data for 1979–2009 except for PWAT from the R1 for which the data is only available after 1994. In addition, diabatic heating fields directly produced by the CFSR for 1979–2009 will be analyzed and compared with that derived based on large-scale fields.

The NCEP R1 and R2 have been widely used for climate studies and their descriptions can be found in Kalnay et al. (1996) for the R1 and Kanamitsu et al. (2002) for the R2. Compared to the R1 and R2, the CFSR includes various upgrades in model physics and assimilation algorithms (Saha et al. 2010). New features in the CFSR include: (1) it is the first reanalysis system in which the guess fields are taken as the 6-h forecast from a coupled atmosphere–ocean climate system with an interactive sea ice component; (2) it uses a higher horizontal resolution ($\sim$38 km) and vertical resolution (64 levels) for the atmosphere than the previous NCEP atmospheric reanalyses; and (3) it assimilates satellite radiances rather than the retrieved temperature and humidity values. The ERAI is described at http://www.ecmwf.int/research/era/do/get/era-interim and its data is available from http://data-portal.ecmwf.int/data/d/interim_daily. Documentations of the MERRA and the related information can be found at http://gmao.gsfc.nasa.gov/research/merra and its data can be obtained from http://disc.sci.gsfc.nasa.gov/daac-bin/DataHoldings.pl.

The analysis is based on daily-mean fields for November to April when the MJO is relatively active. The original observational and reanalysis data are on various spatial grids. For example, the CMORPH rainfall is created at a 0.072° spatial resolution (CMORPH, Joyce et al. 2004) and the NOAA AVHRR is generated twice a day at a 1° spatial resolution (Liebmann and Smith 1996). The reanalysis data are available on a 1.5°×1.5° horizontal grid for ERAI, 0.5°×0.667° grid for MERRA, 2.5°×2.5° grid for NCEP R1 and R2. In this study, all observations and reanalysis data are re-gridded to a common 2.5°×2.5° grid for a consistent comparison.

Anomalies are taken as the departure from seasonal climatology defined as annual mean plus the first 4 harmonics of long-term average. To focus on the intraseasonal variability, most of the analysis will use intraseasonal anomalies obtained by applying 20–100-day band-pass filtering to the raw daily-mean anomalies. Methodologies of the comparison among the reanalyses and observations include the wavenumber-frequency analysis and Empirical Orthogonal Function (EOF) decomposition. The wavenumber-frequency analysis is computed using the software package developed by the U.S. Climate Variability and Predictability (CLIVAR) MJO working group (http://www.usclivar.org/Organization/MJO_WG.html). MJO-related variability is analyzed using composites of MJO events selected based on the two leading EOF modes of the observed intraseasonal OLR anomalies between 30°S and 30°N. The first EOF mode corresponds to a center of the strongest convection variability in the eastern Indian Ocean (EIO) at 97.5°E and the second EOF mode corresponds to a center of the strongest convection variability in the western Pacific at 147.5°E. Temporal evolutions of intraseasonal rainfall, circulation fields, and diabatic heating are diagnosed based on composites for these two centers of the two leading EOF modes.

3 Results

In this section we first compare tropical rainfall variability among three NCEP reanalyses and the CMORPH. MJO-related variability in the NCEP reanalyses is then analyzed based on composites of MJO events, followed by a diagnosis of vertical profiles of diabatic heating in the CFSR. Finally, intraseasonal rainfall variability in ERAI and MERRA is examined.

3.1 Intraseasonal rainfall variability in CMORPH and NCEP reanalyses

Wavenumber-frequency spectra of 10°S–10°N average of raw daily-mean rainfall anomalies from the CMORPH and

NCEP reanalyses for 2000–2009 are shown in Fig. 1. Consistent with the results from previous studies (e.g., CLIVAR Madden–Julian Oscillation Working Group, 2009), spectra in the CMORPH are dominated by eastward propagating components with largest variance confined to 30–100-day periods and wavenumbers 1–3 (Fig. 1a). The amplitude of spectra power in the R1 (Fig. 1b) is too small for identifying the dominance of intraseasonal variability, consistent with the results of Shinoda et al. (1999). The R2 generates larger variance than the R1 but its spectra of intraseasonal eastward wavenumbers 1–3 are also weaker than the observed (Fig. 1c). Further, the R2 produced too much westward variance (especially at high frequencies and large wavenumbers) and the dominance of eastward components is less clear than that in the observation. The distribution of the spectra from the CFSR (Fig. 1d) shows much better similarity to the CMORPH than that from the R1 and R2. In particular, the 30–100-day variance of eastward propagating wavenumber 1–3 in the CFSR is much stronger than that in the R1 and R2.

Intraseasonal (20–100-day band-pass filtered) rainfall anomalies of 10°S–10°N average are compared in Fig. 2 for November 2007 to February 2008 during which MJO activities were exceptionally strong (Janowiak et al. 2010). Two full MJO cycles were observed during this period with large eastward propagating anomalies from the western Indian Ocean to the central Pacific (Fig. 2a). The R1 reproduced the observed features to a certain degree; for examples, the eastward propagating anomalies during active phases that were initiated in early November and mid December 2007 in the western Indian Ocean (Fig. 2b). However, the anomalies in the R1 are rather weak compared to the CMORPH. The amplitude of the anomalies in the R2 is comparable to the observed but their evolutions intermittently appeared to be erroneous (Fig. 2c). The R2 anomalies were not as well organized to propagate from the Indian Ocean to the Pacific as that observed. In fact, the R2 tends to produce more westward propagations such as the positive anomalies between 120°E and 70°E from mid to late November and negative anomalies between the Date Line and 120°E from mid January to mid February 2008. Anomalies from the CFSR (Fig. 2d) are much more realistic compared to the R1 and R2. The CFSR not only captured the observed eastward propagations of each MJO phases but also reproduced the anomalies with reasonable amplitude.

Spatial distribution of temporal correlation with CMORPH is shown in Fig. 3 to examine the overall performance of the reanalyses. The correlation is computed based on daily mean anomalies during November to April

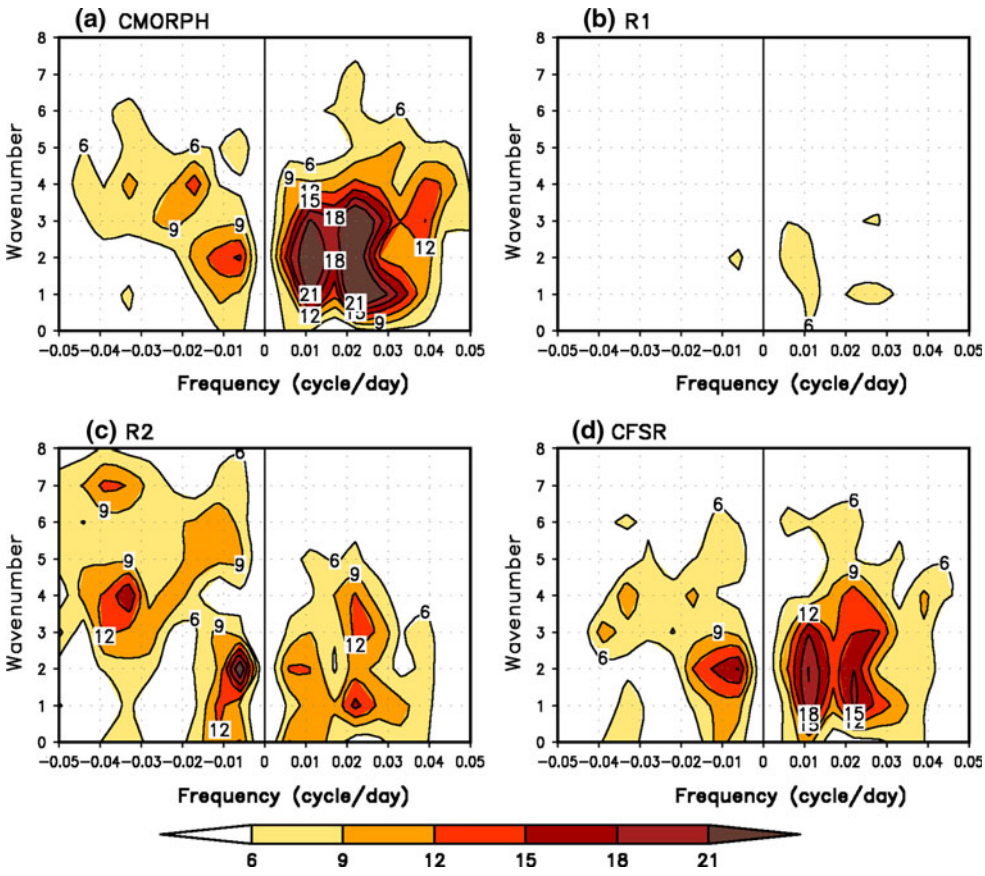

Fig. 1 Wavenumber-frequency spectra of 10°S–10°N average of raw daily–mean anomalies of precipitation. **a** CMORPH; **b** R1; **c** R2; and **d** CFSR. The unit is 0.001 mm^2 $days^{-2}$. Contours are *shaded* starting at 6 with an interval of 3

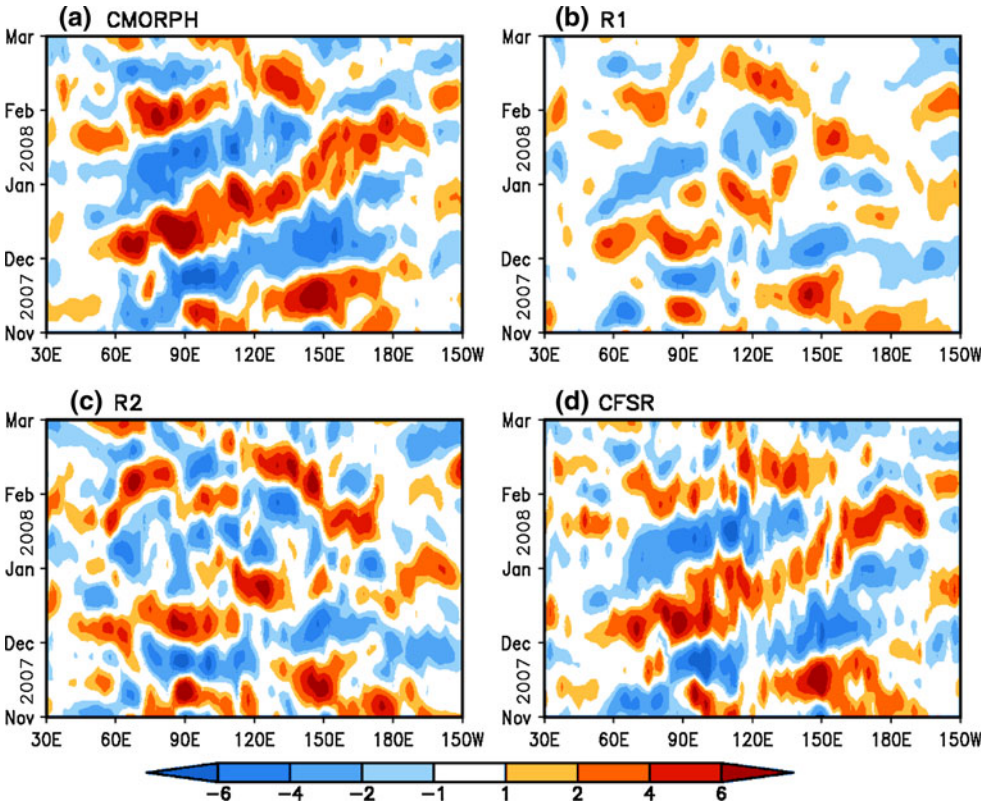

Fig. 2 Time evolution of 10°S–10°N average intraseasonal rainfall for 01 Nov 2007 to 01 Mar 2008. **a** CMORPH; **b** R1; **c** R2; and **d** CFSR. The anomalies are *shaded* starting at ±1, ±2, ±4, and ±6 mm/day

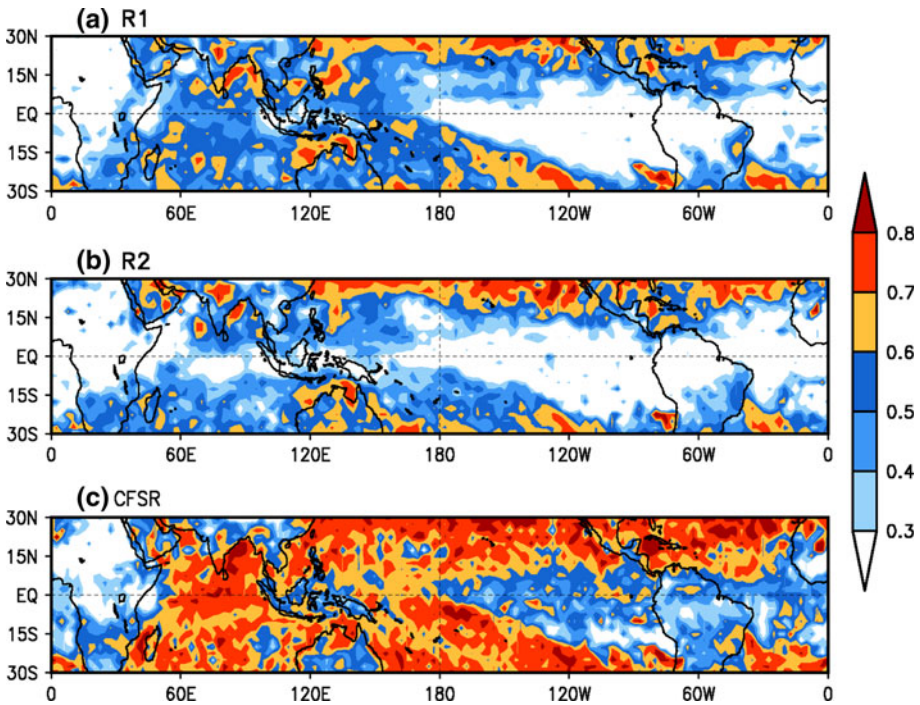

Fig. 3 Correlation of intraseasonal precipitation with CMORPH. **a** R1; **b** R2; and **c** CFSR. Contours are *shaded* starting at 0.3 with 0.1 interval

after intraseasonal filtering. The correlation is generally higher in the subtropical oceans (poleward of 15°N and 15°S) than in the tropical oceans (15°S–15°N). Reasons for this are not clear. Possible explanations may include (1) there are more in situ ship observations for the data assimilations; and (2) the subtropical rainfall is more controlled by large-scale condensation associated with dynamical circulation fields while the tropical rainfall relies on model's representation of both large-scale circulation and deep convection. Within the tropics, the

correlation skill for the R1 is about 0.4–0.6 over the Indian Ocean and western Pacific and less than 0.3 over the rest of the globe (Fig. 3a). The R2 performs worse than the R1 with correlations generally less than 0.4 in the equatorial Indian Ocean and western Pacific (Fig. 3b). Over other tropical regions, the correlations for the R2 are less than 0.3 as those for the R1. The CFSR shows significant improvement over both the R1 and R2 for virtually the entire tropical regions (Fig. 3c). The CFSR correlation is about 0.7 (0.6) or higher over most of the tropical Indian Ocean (western Pacific), where the MJO is most active. Moderate skill of 0.5 or so is also seen from the eastern Pacific eastward through the Atlantic in the CFSR.

Standard deviation of intraseasonal rainfall anomalies is compared in Fig. 4 to assess the strength of the variability. The observation shows relatively large variability over the central to eastern Indian Ocean, western Pacific and the Intertropical Convergence Zones (ITCZs) in the Pacific and Atlantic (Fig. 4a). The amplitude of the intraseasonal variability in the R1 (R2) is smaller (larger) than that in the CMORPH over most of the tropical oceans (Fig. 4c). The amplitude of the variability in the CFSR (Fig. 4d) is more reasonable compared to R1 and R2 over most of the tropics. One deficiency in the CFSR is the too strong amplitude over tropical Africa and South America.

The above results indicate that intraseasonal rainfall variability in the CFSR is significantly improved in representing the dominance of eastward propagation (Fig. 1), phase (Fig. 3) and amplitude (Fig. 4). Since precipitation is not assimilated in these reanalyses and is resulted from the

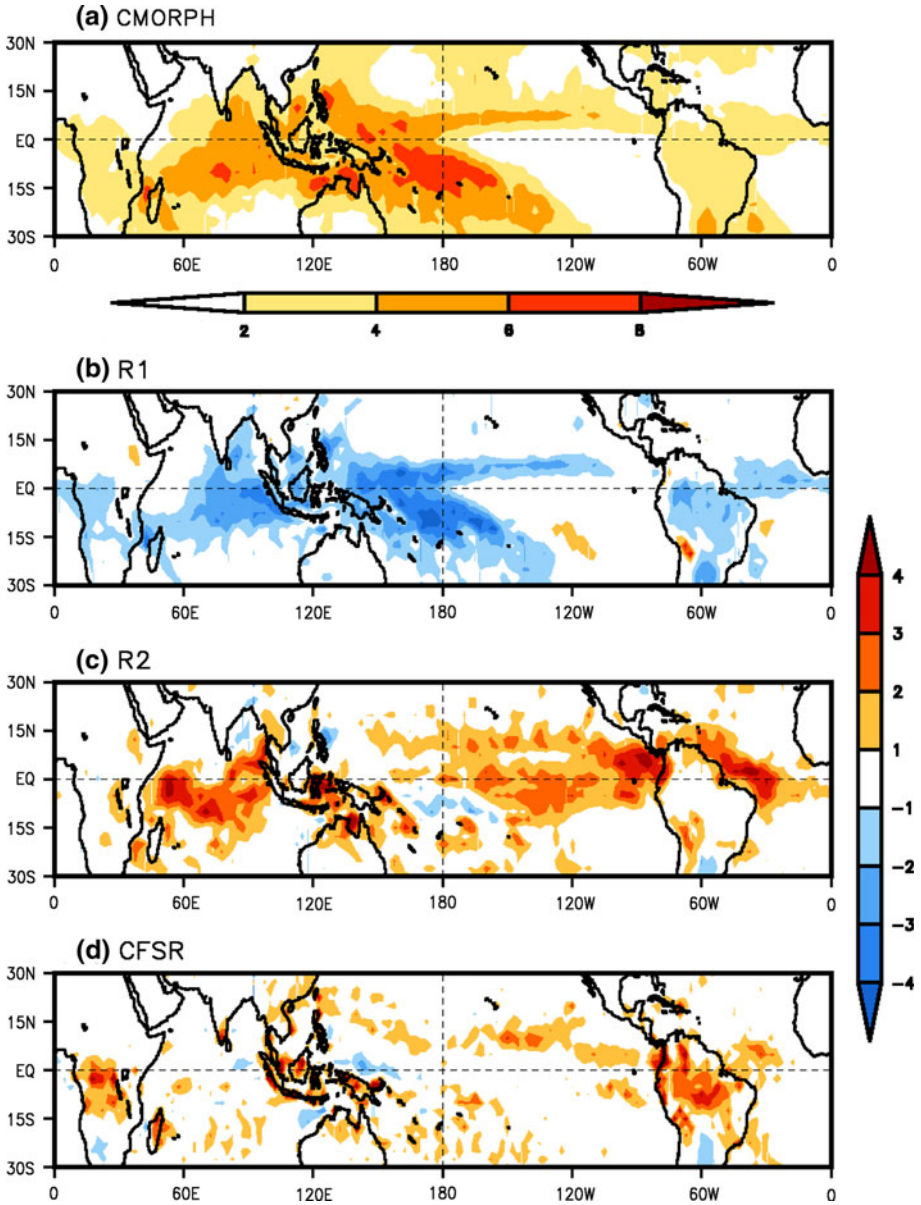

Fig. 4 **a** Standard deviation of intraseasonal rainfall anomalies from CMORPH; **b** differences in standard deviation of intraseasonal rainfall anomalies between R1 and CMORPH; **c** as in **b** except for R2; **d** as in **b** except for CFSR. Contours are *shaded* at an interval of 2 mm/day in **a** and 1 mm/day in **b**–**d** with values between −1 and 1 plotted as *white*

interaction between convection and large-scale circulation, these improvements imply that the large-scale atmospheric fields are also better represented in the CFSR. Although rainfall is not a prognostic variable in numerical models, more accurate large-scale fields associated with improved rainfall are of critical importance in the prediction of intraseasonal variability. Fig. 5 shows standard deviation of 850-hPa convergence which is one of the key factors to precondition the convection through low-level moisture accumulation and accordingly is closely related to rainfall variability. The contrast in the 850-hPa convergence intraseasonal variability among reanalyses (Fig. 5) is consistent with that in rainfall (Fig. 4) with stronger 850-hPa convergence intraseasonal variability corresponding to larger rainfall variability. Over most of the tropical oceans, the amplitude of intraseasonal variability of the 850-hPa convergence in the CFSR is larger than that in the R1 but smaller than that in the R2. Averaged over the domain of Fig. 5 (0–360°E/30°S–30°N), the amplitude is 1.05, 1.46, and 1.30 for the R1, R2, and CFSR. Although the variability in the R2 is strong, its low rainfall correlation with observation (Fig. 4b) suggests that its large-scale dynamical/thermodynamical fields in the R2 are less accurate than that in the CFSR.

3.2 MJO-related variability

In this subsection, we analyze the rainfall variability and its relationships with large-scale fields as well as vertical heating profiles based on composites of MJO events. Principal components of the two leading EOF modes of the observed NOAA AVHRR intraseasonal OLR anomalies are used to select the MJO events. Both the first and the second observed EOF modes are dominated by dipole structures (Fig. 6a, b). In the positive phase of the first EOF mode (EOF1), strongest negative OLR anomalies (enhanced convection) are in the eastern Indian Ocean near the equator and positive OLR anomalies (suppressed convection) in the Pacific south of the equator centered near 180°E (Fig. 6a). In the positive phase of the second EOF mode (EOF2), negative OLR anomalies (enhanced convection) are mostly confined to the eastern Maritime Continent and far western Pacific near the equator and positive OLR anomalies (suppressed convection) in the central Indian (Fig. 6b). The correlation between EOF1 principal component (PC1) and EOF2 principal component (PC2) maximizes at a lead time of 10 days with EOF1 leading EOF2, indicating an eastward propagation of the dominant intraseasonal components. In this study, the combination of EOF1 and EOF2 is taken to represent the MJO.

Two sets of composites are calculated. The first set is with respect to peak positive phase of EOF1 when enhanced convection is centered in the eastern Indian Ocean (EIO) at 97.5°E (Fig. 6a) and the second set with respect to peak positive phase of EOF2 when enhanced convection is centered in the far western Pacific (WPac) at 147.5°E (Fig. 6b). For simplicity, the first (second) set of composites is referred to as EIO (WPac) composite. Conditions for selecting the MJO events for EIO (WPac) composites are: (1) maximum PC1 (PC2) is greater than one standard deviation and (2) amplitude of PC2 (PC1)

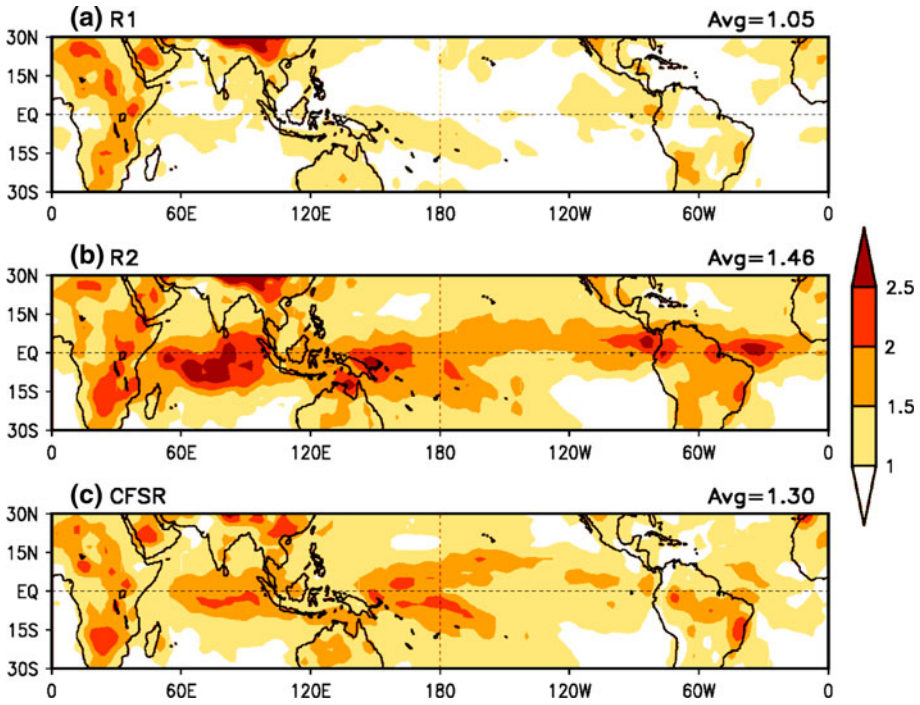

Fig. 5 Standard deviation of 850-hPa convergence intraseasonal anomalies. **a** R1, **b** R2, and **c** CFSR. The unit is 10^{-6} s^{-1}. Contours are *shaded* at starting at 0.5 with an interval of 0.5. Domain average for each reanalysis is given above each panel

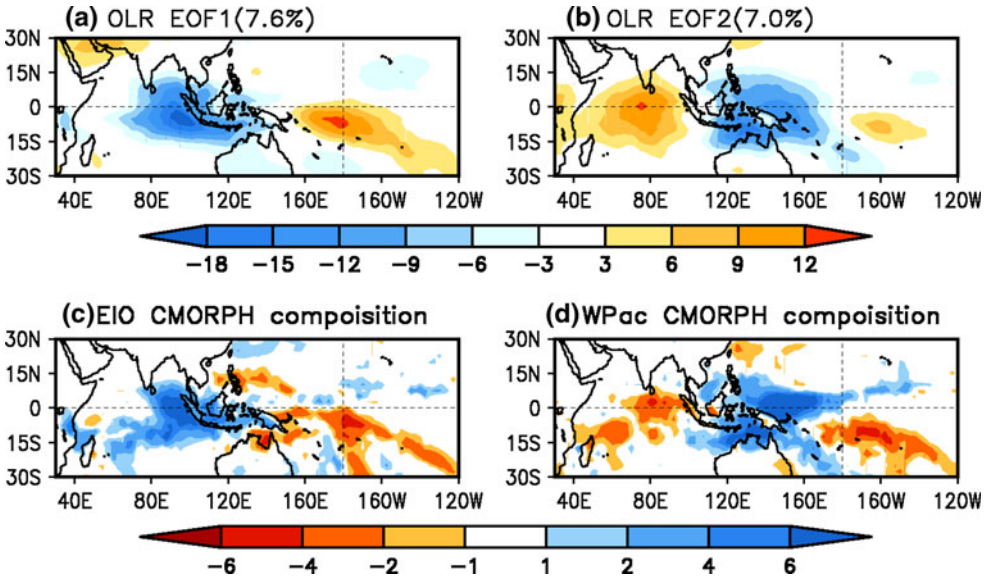

Fig. 6 **a** The first EOF mode (EOF1) of intraseasonal OLR anomalies; **b** as in **a** except for the second EOF mode (EOF2); **c** EIO day-zero composite of CMORPH rainfall of MJO events corresponding to EOF1 when peak intraseasonal convection is in the eastern Indian Ocean; and **d** as in **c** except for WPac composite corresponding to EOF2 when peak intraseasonal convection is in the far western Pacific. Units are arbitrary in **a** and **b** and are mm/day in **c** and **d**. Contours in **c** and **d** are *shaded* at ±1, ±2, ±4, and ±6

8–12 days later (earlier) is greater than 1 standard deviation. The dates of maximum PC1 (PC2) satisfying these two conditions are taken as day zero for EIO (WPac) composites. Visual inspection is also applied to ensure robust eastward propagation of each selected MJO event. For both EIO and WPac composites, these criteria result in a total of 44 events during 1979–2009 and 13 events during 2000–2009.

Spatial distributions of composite intraseasonal CMORPH rainfall anomalies during 2000–2009 are shown in Fig. 6c corresponding to day zero of the EIO composite and Fig. 6d corresponding to day zero of the WPac composite. The CMORPH rainfall composites exhibit similar patterns to the OLR EOF modes (Fig. 6a, b) with enhanced rainfall anomalies in the low latitudes in the EIO (Fig. 6c) and WPac (Fig. 6d).

Figure 7 shows composite intraseasonal 850-hPa wind (vectors) and rainfall anomalies (shadings) from the R1, R2 and CFSR. All three reanalyses produced the observed rainfall patterns with enhanced rainfall in the EIO (eastern Maritime Continent and far WPac) and decreased rainfall to the east of New Guinea (in central eastern Indian Ocean) in EIO (Wpac) composites. Although the overall amplitude of rainfall anomalies in all three reanalyses is weaker than the observed (Fig. 6c, d), the CFSR (Fig. 7c, f) produced strongest rainfall anomalies. In particular, the CFSR captured the decreased rainfall east of Madagascar and in the central Indian Ocean for the WPac composite (Fig. 7f) which are too weak in the R1 and R2 (Fig. 7d, e). Rainfall anomalies in the R1 are the weakest among the three reanalyses, especially for the EIO composite (Fig. 7a). Wind anomalies appeared to be quite similar with westerly anomalies to the west and over the region of enhanced rainfall and easterly anomalies to the east and over the region of decreased rainfall in the tropics. The amplitude of the wind anomalies (shown with contours) indicates that wind anomalies in the R1 are generally slightly weaker than those in the R2 and CFSR. Although the differences in wind anomalies among the reanalyses in Fig. 7 are small, differences in their divergence variability can be substantial.

To analyze more detailed evolutions of rainfall and related fields, we will focus on the composites of 10°S–10°N average at two longitudes where the leading EOF modes show maximum convective variability: EIO composite at 97.5°E and WPac composite at 147.5°E. Temporal evolutions of intraseasonal rainfall anomalies from CMORPH and three NCEP reanalyses together with observed intraseasonal OLR anomalies are shown in Fig. 8a for EIO composites at 97.5°E and Fig. 8b for WPac composite at 147.5°E. Anomalies at negative (positive) lags occur before (after) the observed minimum OLR anomalies at day zero. Observed CMORPH rainfall (black) and OLR (purple) well match each other with maximum rainfall corresponding to minimum OLR, suggesting that both variables are representative of observed convection activities. R2 rainfall anomalies (blue curves) maximize 4 (one) days ahead of the observed in EIO composite at 97.5°E (WPac composite at 147.5°E) with weaker amplitude than the observed in both composites. R1 rainfall leads the observed by 2 days in the EIO composite (Fig. 8a) while being in phase with the observed at the WPac longitude (Fig. 8b). However, the amplitude of rainfall anomalies in the R1 is 2–3 times smaller than the observed. For both the EIO and WPac longitudes, the CFSR rainfall anomalies are stronger than the R1 and R2. One interesting feature in the CFSR composites is that its rainfall anomalies lag the observed by 1 day. Possible

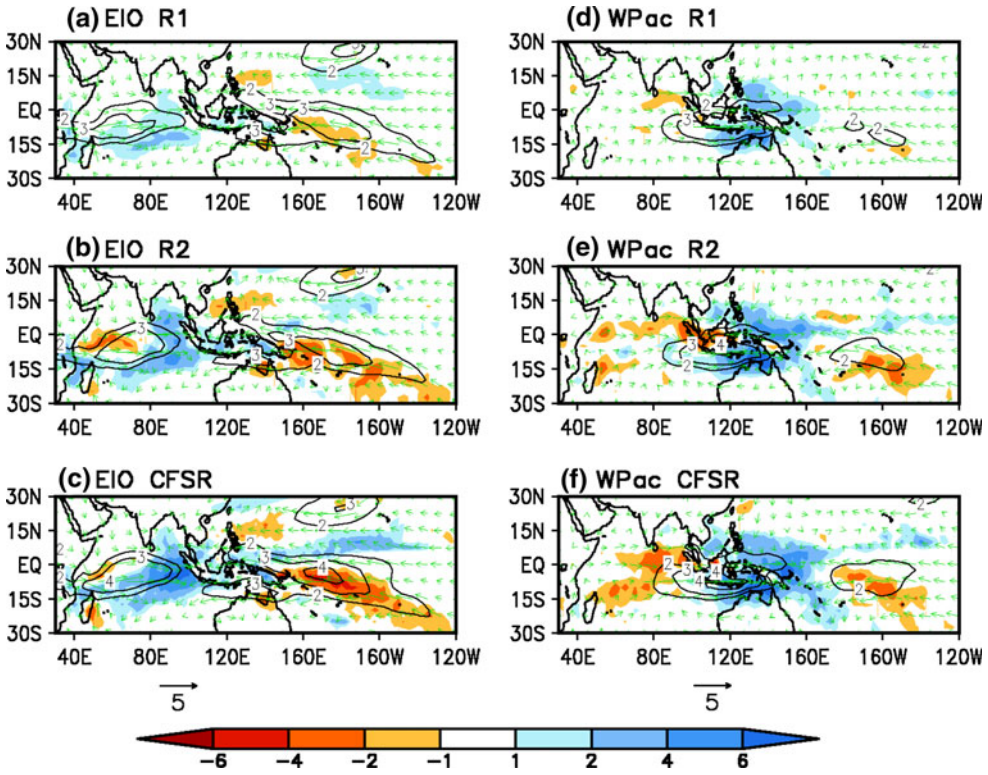

Fig. 7 **a** EIO day-0 composite of rainfall (*shadings*), wind anomaly vector (*arrows*) and wind anomaly amplitude (*contours*) from R1; **b** as in **a** except for WPac; **c** as in **a** except for R2; **d** as in **c** except for WPac; **e** as in **a** except tor CFSR; ad **f** as in **e** except for WPac. Rainfall anomalies are *shaded* at ±1, ±2, ±4, and ±6 mm/day. Scale of wind vectors is indicated below the two *bottom panels* with a unit of m/s. Wind anomalies amplitude is contoured at an interval of 1 m/s

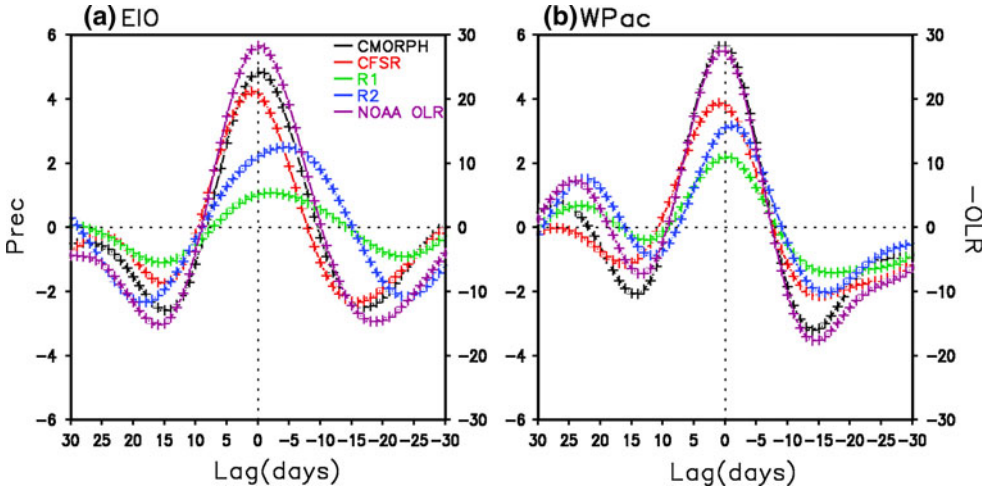

Fig. 8 Evolutions of 10°S–10°N average intraseasonal anomalies for **a** EIO composite at 97.5°E and **b** WPac composites at 147.5°E for CMORPH rainfall (*black*), NOAA OLR (*purple*) R1 rainfall (*green*), R2 rainfall (*blue*), and CFSR rainfall (*red*). Units are mm/day for rainfall (*left y*-axis) and W m^{-2} (*right y*-axis). OLR anomalies are plotted with reversed sign for facilitate the comparison with rainfall. Temporal variations are plotted such that negative (*positive*) lags of the *x*-axis are to the right (*left*) of day zero

reasons for this lag will be discussed in Sect. 4. These characteristics in the reanalyses and observations can also be seen in composites based on longer period from 1979 to 2009.

Next we look at the relationship between inraseasonal rainfall anomalies and large-scale fields. As discussed in the Introduction, various studies have shown the preconditioning of moist middle and lower troposphere before the start of deep convection. Here we analyze the relationship between rainfall and atmospheric PWAT. Evolutions of reanalysis rainfall and PWAT are shown in Fig. 9 based on 1979–2009 data for the R2 and CFSR and 1994–2009 for the R1. Observed OLR anomalies are also included for reference. Maximum PWAT anomalies from the CFSR lead its rainfall maxima by 2–3 days and lead observed minimum OLR by 1–2 days (Fig. 9e, f). In contrast, intraseasonal rainfall anomalies from the R2 in both EIO and WPac composites (Fig. 9c, d) and those from R1 in the WPac composite (Fig. 9b) lead respective PWAT anomalies by 1–2 days. Rainfall and PWAT anomalies from the R1 are about in phase in the EIO composite but the rainfall amplitude is too weak to be considered as a realistic representation of the observed (Fig. 9a). In addition, the composites of maximum PWAT in the WPac composites

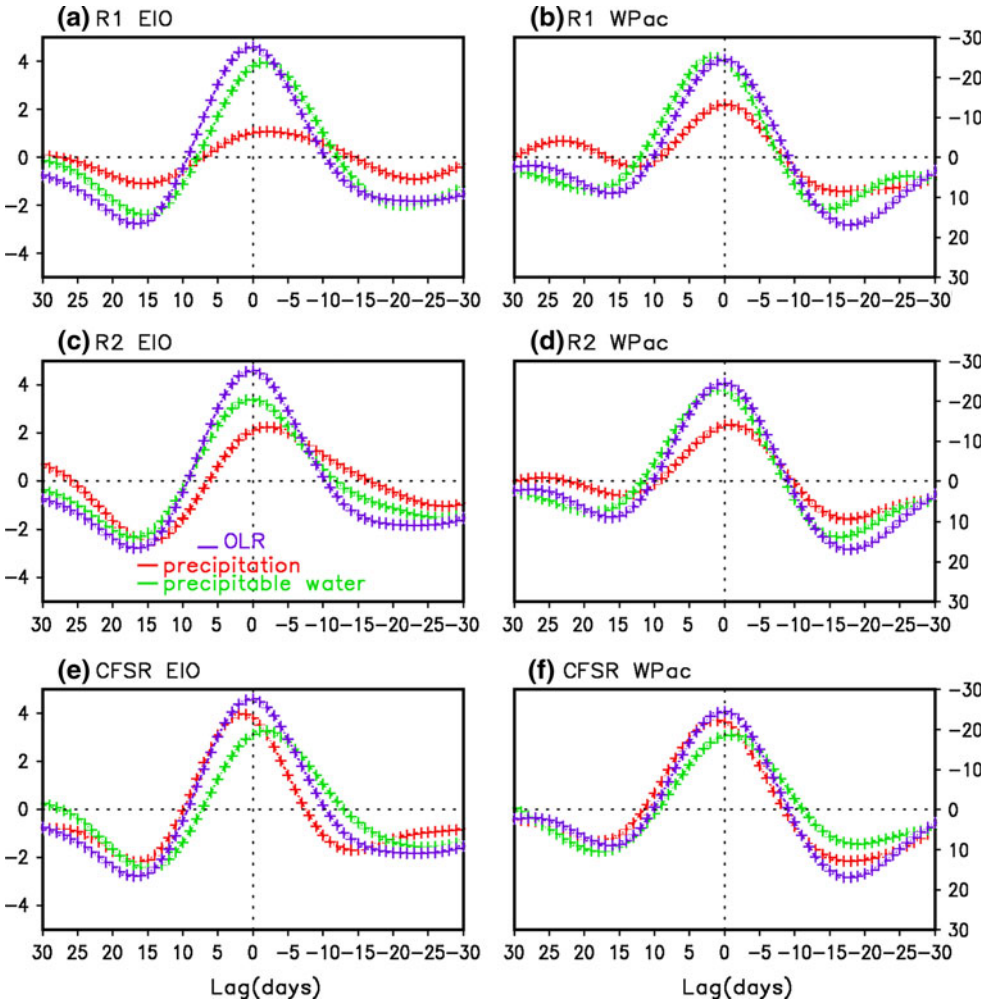

Fig. 9 Composites evolutions 10°S–10°N average intraseasonal anomalies of PWAT (*green*) and rainfall (*red*). **a** EIO composite at 97.5E from R1; **b** WPac composite at 147.5E from R1; **c** as in **a** but for R2; **d** as in **b** but for R2; **e** as in **a** but for CFSR; and **f** as in **b** but for CFSR. For each panel observed intraseasonal OLR anomalies are plotted in *purple*. Units are mm/day for rainfall and mm for PWAT (*left y*-axis) and W m^{-2} for OLR (*right y*-axis). OLR anomalies are plotted with reversed sign for facilitate the comparison with rainfall

from the R1 and R2 lag the observed minimum OLR (Fig. 9b, d) while the maximum PWAT in the R2 in the EIO composite is in phase with observed convection (Fig. 9c).

Large-scale horizontal moisture convergence is an important process in the dynamics of the MJO with moisture convergence contributing to the buildup of moisture static energy ahead of the onset of deep convection and moisture divergence to dry the atmosphere after the passage of the deep convection. Shown in Fig. 10 are composite intraseasonal anomalies of moisture divergence from three NCEP reanalyses at the EIO composites at 97.5°E (Fig. 10a, c, e) and the WPac composites at 147.5°E (Fig. 10b, d, f) based on 1979–2009 data. The moisture divergence is most significantly different among the reanalyses in its amplitude with the R1 being the weakest and the CFSR the strongest. Except for this difference in magnitude, there exist some common features in all three NCEP reanalyses. In the WPac composites, the largest moisture convergence is near the surface, starting 13–15 days and maximizing 2–5 days before the maximum rainfall. Within a few days after the peak convection in the WPac composites, however, moisture convergence is largest between 800 and 900 hPa. The processes of horizontal moisture convergence related to the intraseasonal convection in the eastern Indian Ocean appear to be different. In the EIO composites at 97.5°E, the largest moisture convergence before the maximum rainfall is at 925 hPa or above, rather than near the surface as in the WPac composites, while the convergence immediately after the maximum rainfall shows a maximum near the surface with another maximum at 700 hPa or so. These results suggest that the dynamical processes related to the evolution of the MJO may be different between the Indian Ocean and the western Pacific. The moisture convergence in Fig. 10 consists of contributions from various processes including advection of moisture anomalies by mean horizontal winds, advection of mean moisture by wind anomalies, and moisture advection by transients. Additional studies are needed to further analyze contributions from individual processes.

Diabatic heating is critical in the development and evolution of the MJO through its impacts on the thermodynamic structure of the atmosphere and interactions with large-scale circulations. The availability of heating fields

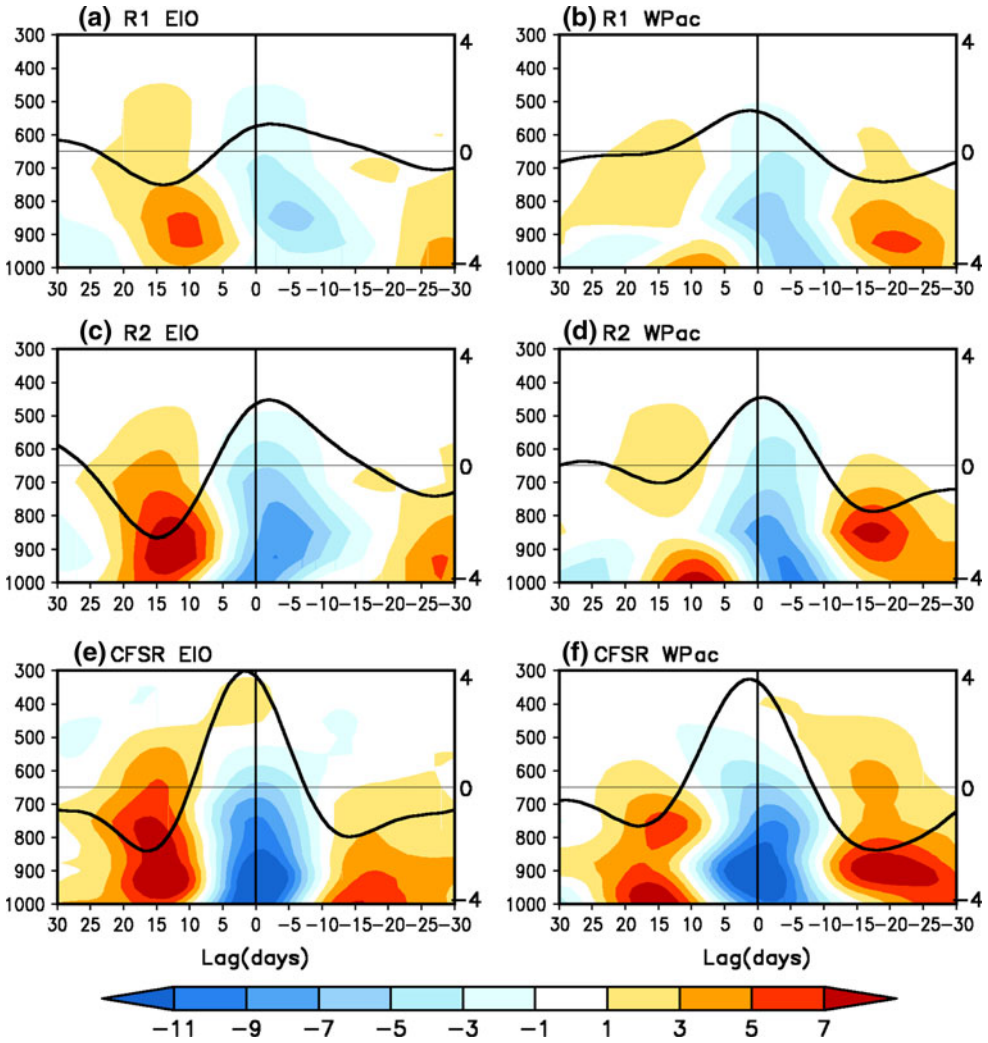

Fig. 10 Composites evolutions 10°S–10°N average intraseasonal anomalies of specific humidity convergence for **a** EIO composite from R1; **b** WPac composite from R1; **c** as in **a** but for R2; **d** as in **b** but for R2; **e** as in **a** but for CFSR; and **f** as in **b** but for CFSR. Corresponding rainfall anomalies are plotted with *black curves* (mm/day, *right y*-axis). Specific humidity convergence is *shaded* at an interval of 2 starting at ±1 with a unit of 10^{-9} s^{-1}

from the CFSR allows us to analyze their variations associated with the MJO. A maximum of total intraseasonal heating anomalies is located between 400 and 500 hPa around the day zero (Fig. 11a, f). During the periods within 7 days before and 10 days after day zero, total heating anomalies are negative throughout most of the atmosphere. These heating anomaly distributions are largely dominated by convection (Fig. 11c, h). The transition from shallow convection and midlevel congests to deep convection ahead of deep convection in previous studies (Johnson et al. 1999; Lin et al. 2004; Benedict and Randall 2007) is not clearly seen in the CFSR. The amplitude of radiation heating anomalies is small with a weak warming near the top of the troposphere around the peak convection near day zero. Stratiform heating anomalies show a westward tilt with height, especially for the WPac composite, with maximum heating between 400 and 500 hPa in the EIO composite (Fig. 11d) and above 400 hPa in the WPac composite (Fig. 11j) a few days after day zero, consistent with the results of Lin et al. (2004).

Due to errors in the model physical parameterizations in reanalysis models, diabatic heating rate in previous studies was estimated based on large-scale fields (Lin et al. 2004; Benedict and Randall 2007). A comparison between the heating fields directly produced from the CFSR and the derived heating rate may help understand the uncertainties in model fields. A total diabatic heating rate is derived using large-scale temperature and velocity fields as in Yanai et al. (1973) and Benedict and Randall (2007). Intraseasonal anomalies of the derived total heating rate are shown in Fig. 11e for EIO composite at 97.5°E and Fig. 11j for WPac composite at 157.5E. Compared to the total heating anomalies from the CFSR model (Fig. 11a, f), the derived heating rate shows larger amplitude than the model produced heating rate around day zero. In the WPac composites, there exist positive anomalies in both model-produced total heating (Fig. 11f) and the derived heating (Fig. 11j) in the lower troposphere 5-10 days before the convection peak at day zero in the WPac composites (Fig. 11f, j) with the derived heating showing larger

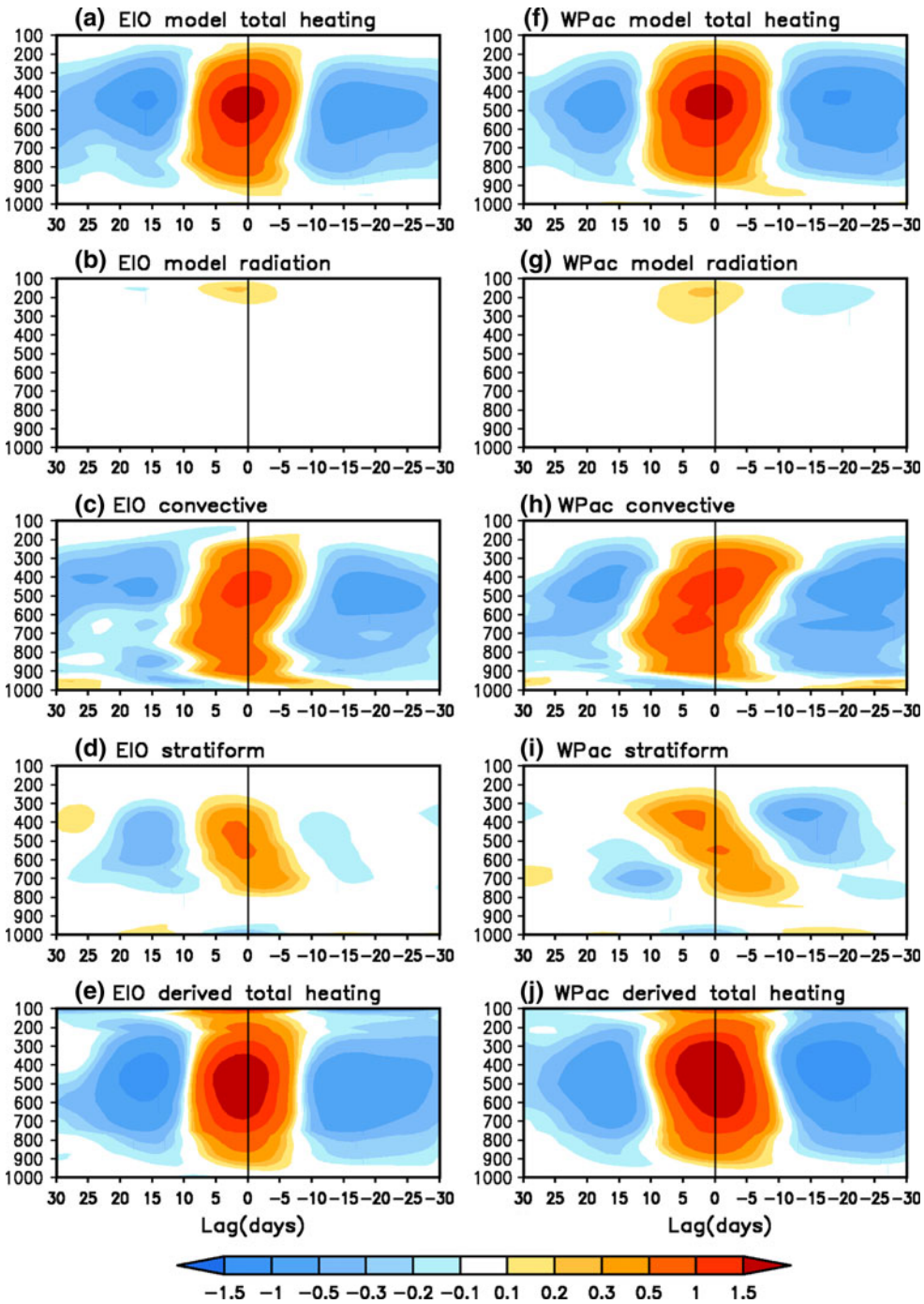

Fig. 11 Composites evolutions 10°S–10°N average intraseasonal anomalies of diabatic heating rate from CFSR. **a** EIO composite of total heating at 97.5E; **b** as in **a** but for radiative heating; **c** as in **a** but for convective heating; **d** as in **a** but for stratiform heating; **e** as in **a** but for derived total heating at 97.5E; **f** WPac composite of total heating at 147.5E; **g** as in **f** but for radiative heating; **h** as in **f** but for convective heating; **i** as in **f** but for stratiform heating; and **j** as in **f** but for derived total heating. Contours are *shaded* at ±0.1, ±0.2, ±0.3, ±0.5, ±1 and ±1.5 K/day

heating anomalies above the planetary boundary layer (PBL, Fig. 11j) while the model-produced heating showing relatively large warming anomalies near the top of the PBL. However, such a warming in the lower troposphere does not clearly exist in the derived heating in EIO composite (Fig. 11e). The heating contrast in the lower troposphere between WPac and WIO is consistent with the results of Ling and Zhang (2011) who found that the low-level heating preceding deep heating in an active phase of the MJO is more likely to be observed over the western Pacific than other locations.

The derived heating rate is computed using analyzed fields produced by the assimilation system by combining the 6-h forecast guess fields and available observations. By definition, the analyzed fields are closer to the truth because of the ingestion of observation in the assimilation. Accordingly, the derived heating rate in Fig. 11e and j is possibly more realistic because of the use of analyzed field.

This argument is consistent with the rainfall comparison (Fig. 8) which shows that the amplitude of rainfall anomalies in the CFSR is weaker than that in the observed estimate (CMORPH).

3.3 Rainfall variability in ERAI and MERRA

Along with the development of the CFSR, two other reanalyses, ERAI and MERRA, have also been produced recently. This subsection assesses the rainfall variability in these two new generation reanalyses. Figure 12a, b show that both the ERAI and MERRA generate stronger rainfall spectra than the R1 (Fig. 1b) and more realistic dominance of eastward propagating variance than R2 (Fig. 1c). The spectra in the MERRA are stronger than those in the ERAI but weaker than those in the CFSR and CMORPH (Fig. 1a, b).

The overall amplitude of intraseasonal variability in ERAI and MERRA is compared with the observation in Fig. 13c, d which show the differences in standard deviation of intraseasonal anomalies from the CMORPH. Consistent with the smaller intraseasonal spectra compared to the CFSR and CMORPH, both ERAI and MERRA show weaker intraseasonal rainfall variability in the tropical eastern Indian Ocean, subtropical southwestern Indian Ocean, and western Pacific. An assessment based on temporal correlations of ERAI and MERRA intraseasonal rainfall with the CMORPH observation is shown in Fig. 13a, b. Both the ERAI and MERRA show significant improvements compared to the R1 and R2 (Fig. 3a, b). It is interesting to notice that although the variability in the ERAI and MERRA is weaker than that in the CFSR, their temporal correlation skill of intraseasonal rainfall is generally comparable to or even locally better than that of the CFSR. Among all reanalyses, the overall correlation skill is highest in the ERAI with an average correlation of 0.66 over 30°S–30°N/0–360°E, compared to 0.40 in R2, 0.42 in R1, and 0.59 in CFSR and MERRA,

4 Discussions

4.1 The rainfall variability

The exact reasons for the differences in the rainfall variability between the CFSR and the previous R1 and R2 are not clear, as there are various changes from the R1 and R2 to the CFSR, including model physics and resolutions, and assimilation algorithms. One possible reason is the change to the treatment of cumulus parameterization. Compared to the scheme used in the R1 (Kalnay et al. 1996) and R2 (Kanamitsu et al. 2002), additional criteria for the onset of convection have been introduced in the NCEP global forecast system (Hong and Pan 1998) which is adopted in the CFSR. These additional criteria require that the convection does not occur until: (1) the level of free convection exists and is within 150 hPa of the parcel's starting level; and (2) cloud depth must be greater than 150 hPa. As suggested in several modeling studies, stronger constraint for convection onset results in a delayed occurrence of convection and stronger tropical intraseasonal variability (Tokioka et al. 1988; Wang and Schlesinger 1999; Lin et al. 2008). However, the small lag of CFSR rainfall from the observed may suggest that the conditions for the onset of convection in the CFSR (Fig. 8), while possibly having improved the representation of intraseasonal variability to some extent, may be a bit too strong, causing a too-long delay of the convection in the CFSR. Such an argument is consistent with the results of the too slow propagation of the MJO simulated with the climate forecast system versions 1 and 2 that uses the same convection parameterization (Pegion and Kirtman 2008; Weaver et al. 2011). Another possible reason for the differences between the CFSR and the previous NCEP R1 and R2 is the use of the much higher vertical resolution of 64 levels for the atmosphere in the CFSR than the R1 and R2 which use 28 levels, which has been shown to enhance intraseasonal

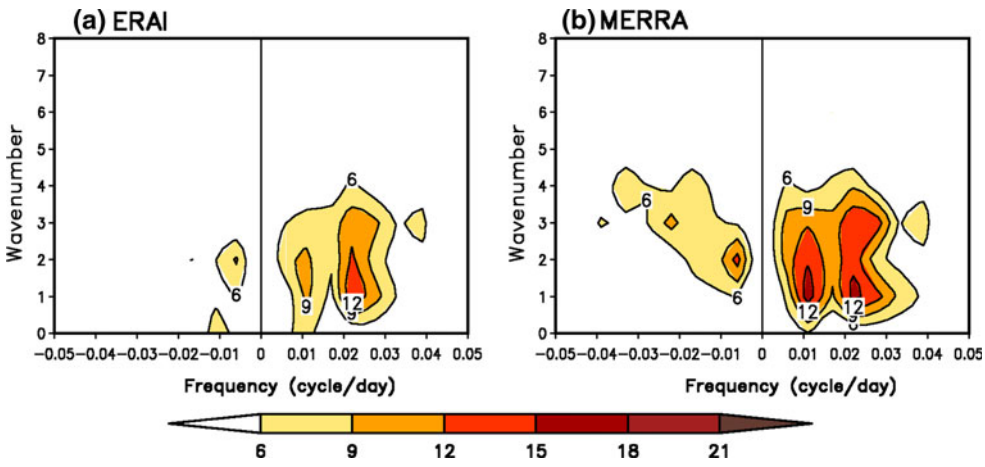

Fig. 12 **a** As in Fig. 1a, except for ERAI; and **b** as in Fig. 1a, except for MERRA

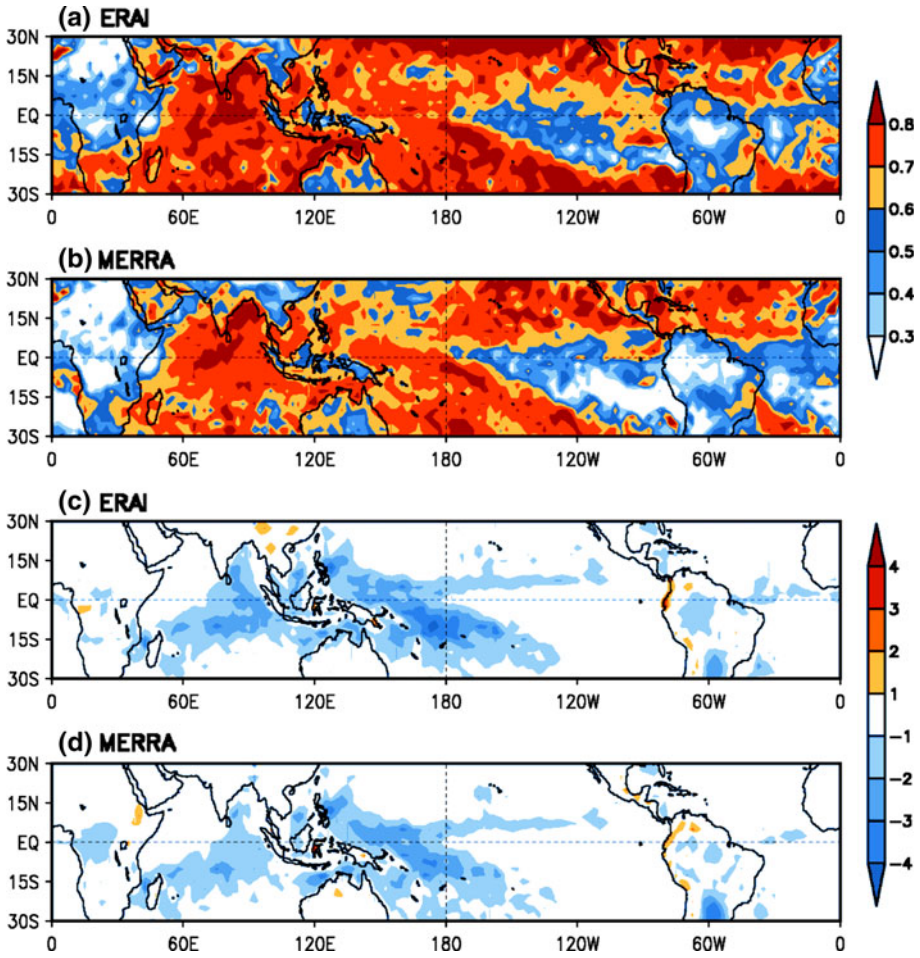

Fig. 13 **a** As in Fig. 3a, except for ERAI; **b** as in Fig. 3a, except for MERRA; **c** as in Fig. 4b, except for ERAI; and **d** as in Fig. 4b, except for MERRA

variability (Inness et al. 2001; van den Dool and Saha 2004).

4.2 Moisture convergence

The differences in the amplitude and vertical distribution of moisture convergence among the NCEP reanalyses indicate that there exist large uncertainties among the reanalyses. Maloney and Hartmann (1998) emphasized the role of frictional convergence near the surface while Kemball-Cook and Weare (2001) showed that the increase in low-level moisture was not caused by the 1,000-hPa convergence. Our results suggest that the relative importance of surface frictional convergence varies spatially. The strong convergence near the surface around the peak convection near day zero in the EIO composites of the R2 and CFSR (Fig. 10c, e) seems to support the finding of Kemball-Cook and Weare (2001) that the convergence lags the moist static energy buildup and is in phase with the convection. It will be helpful to further compare large-scale fields from the CFSR, ERAI and MERRA to examine if discrepancies in moisture convergence among the new generation reanalyses are reduced compared to the earlier products (e.g., R1 and R2). In addition, a decomposition of the total moisture convergence into more specific individual components will help understand the dynamical processes related to the MJO evolution.

4.3 Diabatic heating profiles

While the maximum stratiform heating in the middle-upper troposphere (Fig. 11d, i) is consistent with the results of Lin et al. (2004), its relative contribution to the total diabatic heating is much smaller compared to the observational estimate of Lin et al. (2004) and modeling results of Fu and Wang (2009). Seo and Wang (2010) showed that the relative importance of convective and stratiform heating critically depends on the cumulus parameterization.

The derived heating profiles show a shallow warming leading the convection peak near day zero in the WPac composite. Such a shallow warming is not clear in the EIO composite. Uncertainties in the existence of the shallow warming in the lower troposphere leading the peak convection were also found among TRMM retrievals and global reanalyses (Zhang et al. 2010; Ling and Zhang

2011). More efforts are required to narrow down the uncertainties in both reanalyses and observations.

4.4 Merits of the improved CFSR

Given the mutual interactions between large-scale circulation and convection in the tropics, the improved tropical rainfall variability in the CFSR implies more realistic large-scale fields in these reanalyses. Such an improvement will allow more reliable diagnostic studies to improve our understanding of the physical processes of the tropical intraseasonal variability and provide more accurate initialization for intraseasonal prediction. The development of MJO events and their evolutions have been found to depend on various factors including the preconditioning of deep convection by low-level large-scale moisture advection, shallow convection, saturation fraction of the atmosphere, vertical heating profile, and interactions with the underlying ocean surface. Further detailed comparisons among the new generation reanalyses as well as available in situ observations of these aspects will be helpful for an improved understanding of the MJO mechanisms. It will be interesting to investigate to what extent the initialization with the new reanalyses results in improved prediction.

5 Summary

This study analyzes tropical intraseasonal rainfall variability in several atmospheric reanalyses with a focus on the recently developed National Centers for Environmental Prediction (NCEP) Climate Forecast System Reanalysis (CFSR, Saha et al. 2010). Due to the mutual interactions in the tropical environment and convection, the accuracy of large-scale circulation fields in the atmospheric reanalyses is closely related to their performance in producing rainfall variability. While the large-scale fields from reanalyses have been widely used to study the tropical intraseasonal variability, rainfall variations from the reanalyses have been less focused.

Our analysis shows that intraseasonal rainfall variability in the two previous NCEP reanalyses (R1 and R2) is problematic. The intraseasonal rainfall variations in the R1 are too weak for the identification of any significant intraseasonal variability. The overall amplitude of the intraseasonal rainfall variability in the R2 is comparable to the observation but its temporal evolution becomes erroneous at times with too strong westward propagating disturbances. Compared to the R1 and R2, the CFSR shows significant improvements in intraseasonal rainfall variability including the representation of the dominance of the eastward propagating tropical variance with more realistic amplitude. Spatially, the improvements of the variability are over the entire tropics and subtropics, except for equatorial Africa and South America where the CFSR appears to produce larger variability than the observed. Comparison in low-level convergence variability among the reanalyses is consistent with that in rainfall variability with the R1 (CFSR) producing weakest (strongest) variability.

Rainfall variations and their relationships with large-scale fields in the three NCEP reanalyses are further analyzed using composites of selected Madden-Julian Oscillation (MJO) events based on the two leading EOF modes of the observed outgoing longwave radiation (OLR), which are characterized by strongest convection variability in the eastern Indian Ocean (EIO) centered at 97.5°E in EOF1 and over the eastern Maritime Continent and far western Pacific (WPac) centered at 147.5 in EOF2. Composites for EOF1 and EOF2, referred to as EIO (WPac) composites, are used to analyze MJO-related variability. It is found that maximum intraseasonal rainfall anomalies from the R2 occur ahead of the observed in both EIO and WPac composite. Rainfall anomalies from the R1 also tend to lead the observed in the EIO composite. In contrast, the CFSR rainfall appears to lag the observed by 1 day in both EIO and WPac composites.

Atmospheric PWAT and moisture convergence is analyzed to examine their relationships with rainfall variability. All reanalyses show that positive intraseasonal rainfall anomalies generally correspond to positive anomalies of PWAT. However, while the CFSR shows a lead of PWAT to its own rainfall and observed rainfall, such a relationship is not seen between R1 and R2 PWAT anomalies and their respective rainfall anomalies.

An important aspect in the MJO dynamics is the moisture convergence which contributes to the buildup of moist static energy required for the development of convection (Seo and Kim 2003). A significant difference in moisture convergence among the NCEP reanalyses is that the CFSR produces much stronger anomalies than the R1 and R2. An interesting feature in the moisture convergence is that all NCEP reanalyses show maximum convergence near the surface in the WPac while largest convergence in the EIO is at 925 hPa or above, suggesting that different physical processes may contribute to the development and evolution of the MJO in different regions.

Vertical heating profiles show that the diabatic heating in the CFSR is dominated by convection. Stratiform condensation also contributed to the total heating with a clear westward tilt and maximum warming anomalies between 400 and 500 hPa following the maximum rainfall anomalies in the observation and CFSR, consistent with the previous observational analysis (Lin et al. 2004). Total heating anomalies from the CFSR have similar temporal and vertical structure to those derived based on large-scale fields

but with the heating anomalies from the CFSR being weaker than the derived.

Rainfall variability from the other two recently produced reanalyses, the ECMWF Re-Analysis Interim (ERAI), and the Modern Era Retrospective-analysis for Research and Applications (MERRA), is also analyzed. It is shown that both the ERAI and MERRA generate stronger rainfall spectra than the R1 and more realistic dominance of eastward propagating variance than R2. The intraseasonal variability MERRA is stronger than that in the ERAI but weaker than that in the CFSR and CMORPH.

Acknowledgments Leigh Zhang helped offload and prepare MERRA data. We greatly appreciate the constructive internal reviews by Huug van den Dool and FangLin Yang. XH Fu is supported by JAMSTEC, NOAA, and NASA through the IPRC, whose contribution is as IPRC No. 780 and SOEST No. 8143. KH Seo was funded by the Korea Meteorological Administration Research and Development Program under Grant CATER 2007-4208.

References

Agudelo PA, Curry JA, Hoyos CD, Webster PJ (2006) Transition between suppressed and active phases of intraseasonal oscillations in the Indo-Pacific warm pool. J Clim 19:5519–5530

Benedict JJ, Randall DA (2007) Observed characteristics of the MJO relative to maximum rainfall. J Atmos Sci 64:2332–2354. doi:10.1175/JAS3968.1

Chang CP, Lim H (1988) Kelvin wave-CISK: a possible mechanism for the 30–50-day oscillations. J Atmos Sci 45:1709–1720

CLIVAR Madden–Julian Oscillation Working Group (2009) MJO simulation diagnostics. J Clim 22:3006–3030. doi:10.1175/2008JCLI2731.1

Fu X, Wang B (2009) Critical role of stratiform rainfall in sustaining the Madden-Julian Oscillation: GCM experiments. J Clim 22:3939–3959. doi:10.1175/2009JCLI2610.1

Fu X, Wang B, Bao Q, Liu P, Lee JY (2009) Impacts of initial conditions on monsoon intraseasonal forecasting. Geophys Res Lett 36:L08801. doi:10.1029/2009GL037166

Fu X, Wang B, Lee JY, Wang W, Gao L (2010) Better initial conditions significantly improve intraseasonal prediction. Mon Weather Rev (submitted)

Hendon HH, Liebmann B, Newmann M, Glick JD, Schemm JE (2000) Medium-range forecast errors associated with active episodes of the Madden-Julian Oscillation. Mon Weather Rev 128:69–86

Hong SY, Pan HL (1998) Convective trigger function for a mass-flux cumulus parameterization scheme. Mon Weather Rev 126: 2599–2620

Inness PM, Slingo JM, Woolnough SJ, Neale RB, Pope VD (2001) Organization of tropical convection in a GCM with varying verticalresolution: implications for the simulation of the Madden–Julian oscillation. Clim Dyn 17:777–793

Janowiak JE, Bauer P, Wang W, Arkin PA, Gottschalck J (2010) An evaluation of precipitation forecasts from operational models and reanalyses including precipitation variations associated with MJO activity. Mon Weather Rev 138:4542–4560

Jiang X, Waliser DE, Olson WS, Tao WK, L'Ecuyer TS, Li JL, Tian BJ, Yung YL, Tompkins AM, Lang SE, Grecu M (2009) Vertical heating structures associated with the MJO as characterized by TRMM estimates, ECMWF reanalyses and forecasts: a case study during 1998–99 winter. J Clim 22:6001–6020. doi:10.1175/2009JCLI3048.1

Johnson RH, Rickenbach TM, Rutledge SA, Ciesielski PE, Schubert WH (1999) Trimodal characteristics of tropical convection. J Clim 12:2397–2418

Jones C, Carvalho LMV, Higgins RW, Waliser DE, Schemm JKE (2004) A statistical forecast model of tropical intraseasonal convective anomalies. J Clim 17:2078–2095. doi:10.1175/1520-0442(2004)017

Joyce RJ, Janowiak JE, Arkin PA, Xie P (2004) CMORPH: a method that produces global precipitation estimates from passive microwave and infrared data at high spatial and temporal resolution. J Hydrometeoro 5:487–503

Kalnay E, et al (1996) The NCEP/NCAR 40-Year Reanalysis Project. Bull Am Meteor Soc 77:437–471

Kanamitsu M, Ebisuzaki W, Woolen J, Yang SK, Hnilo J, Fiorino M, Potter GL (2002) NCEP–DOE AMIP-II Reanalysis (R-2). Bull Am Meteor Soc 83:1631–1643

Kang IS, Kim HM (2010) Assessment of MJO predictability for boreal winter with various statistical and dynamical models. J Clim 23:2368–2378. doi:10.1175/2010JCLI3288.1

Kemball-Cook S, Weare BC (2001) The onset of convection in the Madden-Julian Oscillation. J Clim 14:780–793

Kim D, Sperber K, Stern W, Waliser D, Kang I, Maloney E, Wang W, Weickmann K, Benedict J, Khairoutdinov M (2009) Application of MJO simulation diagnostics to climate models. J Clim 22:6413–6436. doi:10.1175/2009JCLI3063.1

Lau KM, Peng L (1987) Origin of low-frequency (intraseasonal) oscillations in the tropical atmosphere. Part I: Basic theory. J Atmos Sci 44:950–972

Li C, Jia X, Ling J, Zhou W, Zhang C (2009) Sensitivity of MJO simulations to convective heating profiles. Clim Dyn 32:167–187

Liebmann B, Smith CA (1996) Dscription of a complete (interpolated) outgoing longwave radiation dataset. Bull Am Meteor Soc 77:1275–1277

Lin JL, Mapes BE, Zhang MH, Newman M (2004) Stratiform precipitation, vertical heating profiles, and the Madden–Julian oscillation. J Atmos Sci 61:296–309

Lin JL, Kiladis GN, Mapes BE, Weickmann KM, Sperber KR, Lin WY, Wheeler M, Schubert SD, Genio AD, Donner LJ, Emori S, Gueremy JF, Hourdin F, Rasch PJ, Roeckner E, Scinocca JF (2006) Tropical intraseasonal variability in 14 IPCC AR4 climate models. Part I: Convective signals. J Clim 19:2665–2690

Lin JL, Lee MI, Kim D, Kang IS, Frierson D (2008) The impacts of convective parameterization and moisture triggering on AGCM-simulated convectively coupled equatorial waves. J Clim 21:883–909. doi:10.1175/2007JCLI1790.1

Ling J, Zhang C (2011) Structural evolution in heating profiles of the MJO in global reanalyses and TRMM retrievals. J Clim 24:825–842. doi:10.1175/2010JCLI3826.1

Maloney E, Hartmann D (1998) Frictional moisture convergence in a composite life cycle of the Madden–Julian oscillation. J Clim 11:2387–2403

Pegion K, Kirtman B (2008) The impact of Air–Sea interactions on the predictability of the tropical intraseasonal oscillation. J Clim 21:5870–5886

Saha S et al (2006) The NCEP climate forecast system. J Clim 19:3483–3517

Saha S et al (2010) The NCEP climate forecast system reanalysis. Bull Am Meteor Soc 8:1015–1058. doi:10.1175/2010BAMS3001.1

Seo KH, Kim KY (2003) Propagation and initiation mechanisms of the Madden-Julian oscillation. J Geophys Res 108:4384–4405

Seo KH, Wang W (2010) The Madden-Julian oscillation simulated in the NCEP climate forecast system model: the importance of

stratiform heating. J Clim 23:4770–4793. doi:10.1175/2010JCLI2983.1

Seo KH, Wang W, Gottschalck J, Zhang Q, Schemm JKE, Higgins WR, Kumar A (2009) Evaluation of MJO forecast skill from several statistical and dynamical forecast models. J Clim 22:2372–2388. doi:10.1175/2008JCLI2421.1

Shinoda T, Hendon HH, Glick J (1999) Intraseasonal surface fluxes in the tropical western Pacific and Indian Oceans from NCEP reanalysis. Mon Weather Rev 127:678–693

Tokioka T, Yamazaki K, Kitoh A, Ose T (1988) The equatorial 30–60-day oscillation and the Arakawa-Schubert penetrative cumulus parameterization. J Meteor Soc Jpn 66:883–901

van den Dool H, Saha S (2004) Analysis of propagating modes in the tropics in short AMIP runs. In: Proceedings of the WCRP/WGNE workshop on the second phase of the atmospheric model intercomparison project (AMIP2), Meteo-France, Toulouse, France 11.14 November, 2002, pp 87–91. (Edited by P. Gleckler August 16, 2004, UCRL-PROC-209115)

Waliser DE, Lau KM, Stern W, Jones C (2003) Potential predictability of the Madden–Julian oscillation. Bull Am Meteor Soc 84:33–50

Wang W, Schlesinger ME (1999) The dependence on convection parameterization of the tropical intraseasonal oscillation simulated by the UIUC 11-layer atmospheric GCM. J Clim 12:1423–1457

Wang W, Xie P, Yoo SH, Xue Y, Kumar A, Wu X (2010) An assessment of the surface climate in the NCEP climate forecast system reanalysis. Clim Dyn, doi:10.1007/s00382-010-0935-7

Weaver SJ, Wang W, Chen M, Kumar A (2011) Representation of MJO variability in the NCEP climate forecast system. J Clim (submitted)

Wu R, Kirtman BP, Pegion K (2008) Local rainfall-SST relationship on subseasonal time scales in satellite observations and CFS. Geophys Res Lett 35:L22706. doi:10.1029/2008GL035883

Yanai M, Esbensen S, Chu JH (1973) Determination of bulk properties of tropical cloud clusters from large-scale heat and moisture budgets. J Atmos Sci 30:611–627

Zhang C (2005) Madden-Julian Oscillation. Rev Geophys 43:1–36, RG2003. doi:10.1029/2004RG000158

Zhang C, Dong M, Gualdi S, Hendon HH, Maloney ED, Marshall A, Sperber KR, Wang W (2006) Simulations of the Madden-Julian oscillation in four pairs of coupled and uncoupled global models. Clim Dyn 27:573–592

Zhang C, Ling J, Hagos S, Tao WK, Lang S, Takayabu YN, Shinge S, Katsumata M, Olson WS, L'Ecuyer T (2010) MJO signals in latent heating: results from TRMM retrievals. J Atom Sci 67:3488–3508. doi:10.1175/2010JAS3398.1